optical spectrum analyzer, respectively. The operating process is the same as the experiment which has been described earlier in Section 4. The theoretical and experimental macrobending loss curves versus wavelength ranging from 1500 to 1600 nm for bend radius of 6.5 and 6 mm are presented in Figures 6(a) and 6(b), respectively, from which one can see that the theoretical bend loss agrees with the experimental results. As a comparison, the measured bend losses of bare SMF28 in Figure 5 are also presented. The difference of bend loss between the two cases, i.e., bare SMF28 and the bare SMF28 with an absorbing layer, shows that the reflection occurring at the interface between the cladding layer and air has a significant effect on the bend loss.

6. CONCLUSION

In conclusion, we have presented a thorough theoretical and experimental investigation of the macrobending loss characteristics of a standard single mode fiber with small bend radii, which includes theoretical modeling analysis for fiber bend loss, for SMF28 with coating layers and the bare SMF28 after stripping the coating layers and chemical etching of partial cladding. Both experimental and theoretical results have demonstrated the impact of reflection occurring at the interface between the cladding and coating layer or the cladding layer and air on the bend loss.

REFERENCES

1. N. Lagakos, T. Litovitz, P. Macedo, R. Mohr, and R. Meister, Multimode optical fiber displacement sensor, Appl Opt 20 (1981), 167–176.
2. N. Lagakos, J.H. Cole, and J.A. Bucaro, Microbend fiber-optic sensor, Appl Opt 26 (1987), 2171–2180.
3. M.T. Wlodarczyk, Wavelength referencing in single-mode microbend sensors, Opt Lett 12 (1987), 741–743.
4. R.C. Gauthier and C. Ross, Theoretical and experimental considerations for a single-mode fiber-optic bend-type sensor, Appl Opt 36 (1997), 6264–6273.
5. Y. Jeong, S. Baek, B. Lee, S. Choi, and K. Oh, Macrobend sensor via the use of a hollow-core splice fiber: Theory and experiments, Opt Eng 41 (2002), 1815–1820.
6. S.H. Nam and S. Yin, High-temperature sensing using whispering gallery mode resonance in bent optical fibers, IEEE Photon Technol Lett 17 (2005), 2391–2393.
7. D. Marcuse, Curvature loss formula for optical fibers, J Opt Soc Am 66 (1976), 216–220.
8. D. Marcuse, Bend loss of slab and fiber modes computed with diffraction theory, IEEE J Quantum Electron 29 (1993), 2957–2961.
9. C. Vassallo, Perturbation of an LP mode of an optical fiber by a quasi-degenerate field: A simple formula, Opt Quantum Electron 17 (1985), 201–205.
10. I. Valiente and C. Vassallo, New formalism for bending losses in coated single-mode optical fibers, Electron Lett 25 (1989), 1544–1545.
11. H. Renner, Bending losses of coated single-mode fibers: A simple approach, J Lightwave Technol 10 (1992), 544–551.
12. L. Faustini and G. Martini, Bend loss in single-mode fibers, J Lightwave Technol 15 (1997), 671–679.
13. Y. Powell-Friend, L. Phillips, T. George, and A. Sharma, A simple technique for investigating whispering gallery modes in optical fibers, Rev Sci Instrum 69 (1998), 2868–2870.
14. Q. Wang, G. Farrell, and T. Freir, Theoretical and experimental investigations of macro-bend losses for standard single mode fibers, Opt Exp 13 (2005), 4476–4484.
15. Q. Wang, G. Farrell, T. Freir, G. Rajan, and P. Wang, Low-cost wavelength measurement based on a macrobending singlemode Fiber, Opt Lett 31 (2006), 1785–1787.

ON THE DESIGN OF MULTIFREQUENCY DIVIDERS SUITABLE FOR GSM/DCS/PCS/UMTS APPLICATIONS BY USING A PARTICLE SWARM OPTIMIZATION-BASED TECHNIQUE

Zaharias D. Zaharis,[1] Dimitra G. Kampitaki,[1] Pavlos I. Lazaridis,[1,2] Anastasia I. Papastergiou,[1] and Philippe B. Gallion[2]
[1] Department of Electronics, Alexander Technological Educational Institute of Thessaloniki, 57400 Thessaloniki, Greece
[2] Département Communications et Electronique, Unité de Recherche Associée au Centre National de la Recherche Scientifique, 820 Ecole Nationale Supérieure des Télécommunications, 46 rue Barrault, 75634 Paris Cedex 13, France

Received 19 February 2007

ABSTRACT: *A particle swarm optimization-based technique is applied to design dividers that operate in two or more frequency bands at once. The geometry of the dividers is optimized under specific requirements concerning the impedance-matching bandwidth and the complex current distribution on unmatched real or complex terminal loads for each one of the resonant frequencies. The required current distribution on the loads concerns not only the ratio between the current amplitudes but also the phase difference between the currents. Several cases are studied to show the robustness of the particle swarm optimizer as well as the ability of the technique to derive optimal multifrequency structures suitable for GSM/DCS/PCS/UMTS applications.* © 2007 Wiley Periodicals, Inc. Microwave Opt Technol Lett 49: 2138–2144, 2007; Published online in Wiley InterScience (www.interscience.wiley.com). DOI 10.1002/mop.22658

Key words: *multifrequency dividers; multiband dividers; multiband mobile antennas; mobile communications; particle swarm optimization*

1. INTRODUCTION

Dividers are structures of great interest, especially for feeding networks of wireless or mobile communications systems [1–3]. The two main purposes of a divider are splitting the signal according to the desired split ratio and providing impedance matching inside the frequency range of operation [4]. Of course, a well-designed divider must satisfy an additional requirement concerning the desired phase difference between the signals applied on the terminal loads. So far, many methods have been proposed for the designing of dividers that satisfy the above requirements [5–29]. Most of these methods consider dividers operating in a single frequency band. However, the need for simultaneous operation in two or more frequency bands led to the designing of dual-frequency [28, 29] or multifrequency dividers.

A multifrequency divider must satisfy the earlier-mentioned requirements concerning the desired impedance-matching bandwidth and the desired signal-split ratio, including the phase difference between the signals applied on the terminal loads. The main difficulty in designing such a divider results from the fact that all the above requirements must be satisfied simultaneously in all the frequency bands, considering that the terminal loads are not matched to the main transmission line that feeds the divider. In addition, a multifrequency divider that complies with the above requirements must be easily implemented in practice.

To overcome the above difficulties, the present work introduces a new technique, which makes use of a particle swarm optimization-(PSO) based algorithm developed by the authors. The fundamentals of PSO have been discussed in many papers [30–39] and many problems have already been solved by applying PSO-based methods

[40–58]. According to our technique, the geometry of the divider is analyzed by using transmission line theory [59–62]. The results derived from the analysis are the impedance-matching bandwidth, the ratio between the amplitudes of the currents applied on the terminal loads, and the phase difference between these currents. The values of the above parameters are used for the estimation of a suitably defined mathematical expression called "fitness function." The basic idea implemented by the PSO algorithm is to maximize the fitness function. The fitness function achieves its global maximum when the above parameters reach their desired values. The geometry of the divider, that produces the fitness global maximum, is the optimum solution to the specific designing problem.

The proposed technique has been applied to optimize dividers for GSM/DCS operation and also for GSM/DCS/PCS/UMTS operation. Several cases were studied in this work with different values of current-split ratio at the terminal points of the divider and with different real or complex values of terminal loads. The results show that the technique is very effective and very useful in practice, because the resulting structures are realistic and can be fabricated by using microstrip technology.

2. FORMULATION

The proposed structure of the divider consists of two branches that feed two corresponding terminal loads, Z_{AT} and Z_{BT}, as shown in Figure 1. The loads may be real or complex and are generally not

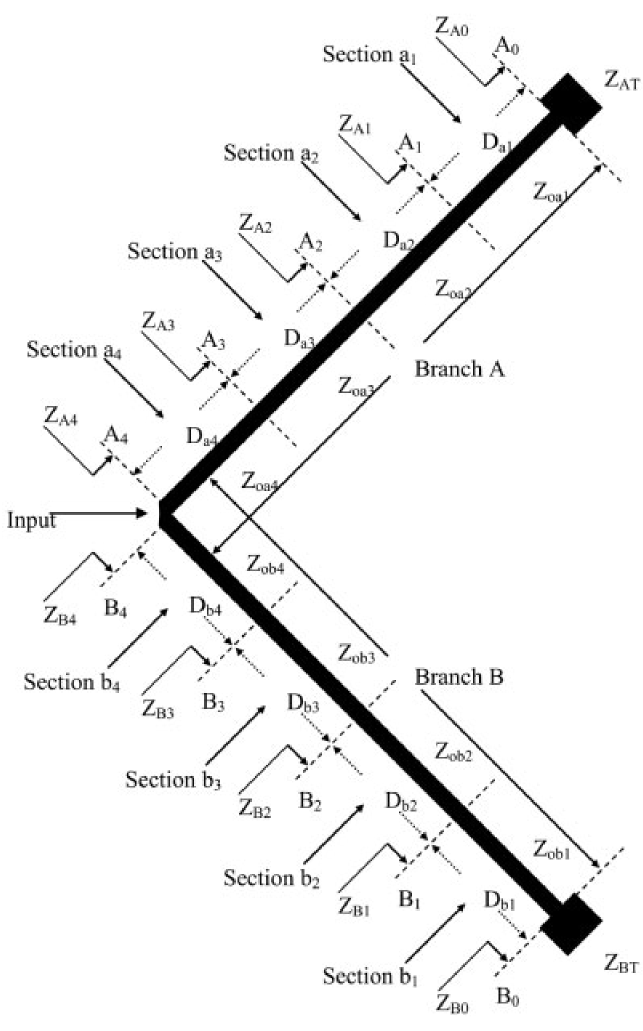

Figure 1 The proposed structure of the multifrequency divider

matched to the main line that feeds the divider. Two types of parameters define the geometry of the divider: lengths and the characteristic impedances of the transmission lines used for the construction of the branches. The optimization of a structure under many constraints demands a geometry defined by many parameters. Every parameter can be considered as a degree of freedom available to optimize the divider. Therefore, each branch is assumed to be composed of tandem transmission line sections of different length and of different characteristic impedance. After several trials, it was found that four sections per branch are sufficient to optimize the divider. In particular, the branch A consists of four sections with lengths D_{a1}, D_{a2}, D_{a3}, D_{a4} and corresponding characteristic impedances Z_{oa1}, Z_{oa2}, Z_{oa3}, Z_{oa4}. Similarly, the branch B consists of four sections with lengths D_{b1}, D_{b2}, D_{b3}, D_{b4} and corresponding characteristic impedances Z_{ob1}, Z_{ob2}, Z_{ob3}, Z_{ob4}. In total, there are 16 optimization parameters available to optimize the divider. Because of the stochastic nature of the optimization procedure, each one of the above parameters may take any real value. Therefore, it is desirable to fabricate the divider in microstrip form. The microstrip technology provides the advantage of fabricating the sections of the divider with any value of length and any value of characteristic impedance.

As mentioned earlier, a well-designed divider has to achieve the desired impedance-matching bandwidth (BW), meaning that the input impedance of the divider has to be as close as possible to the characteristic impedance of the main feeding line inside the frequency range of operation [4]. Actually, the impedance-matching bandwidth is the frequency range where the return loss (RL) is below -9.54 dB (approximately -10 dB). A way of calculating the RL is given below. The value of the terminal load Z_{AT} coincides with the input impedance at the position A_0:

$$Z_{A0} = Z_{AT} \tag{1}$$

The input impedance at the position A_i ($i = 0, \ldots, 3$) is considered to be the terminal load of the section a_{i+1}. Using transmission line theory [59–62], the input impedances at the positions A_i ($i = 1, \ldots, 4$) are calculated recursively by the following expression:

$$Z_{Ai} = Z_{oa1}\frac{Z_{A(i-1)} + jZ_{oai}\tan(\beta D_{ai})}{Z_{oai} + jZ_{A(i-1)}\tan(\beta D_{ai})} \tag{2}$$

where β is the phase constant inside the microstrip structure of the divider and $Z_{A(i-1)}$ is the input impedance at the position A_{i-1}. Similarly, the value of the terminal load Z_{BT} coincides with the input impedance at the position B_0:

$$Z_{B0} = Z_{BT} \tag{3}$$

The input impedance at the position B_i ($i = 0, \ldots, 3$) is considered to be the terminal load of the section b_{i+1}. Thus, the input impedances at the positions B_i ($i = 1, \ldots, 4$) are calculated recursively by the following expression:

$$Z_{Bi} = Z_{obi}\frac{Z_{B(i-1)} + jZ_{obi}\tan(\beta D_{bi})}{Z_{obi} + jZ_{B(i-1)}\tan(\beta D_{bi})} \tag{4}$$

where $Z_{B(i-1)}$ is the input impedance at the position B_{i-1}. The position A_4 is identical with B_4. Therefore, the input impedance Z_{in} of the divider is the parallel combination of Z_{A4} and Z_{B4}:

$$Z_{in} = (Z_{A4}^{-1} + Z_{B4}^{-1})^{-1} \tag{5}$$

The main line that feeds the divider is considered to have a characteristic impedance of 50 Ω. Then, the RL at the input of the divider is calculated in decibels as follows:

$$\mathrm{RL} = 20\log\left|(Z_{\mathrm{in}} - 50)/(Z_{\mathrm{in}} + 50)\right|[\mathrm{dB}] \tag{6}$$

Another important factor is the current-split ratio (CR), which is defined as the ratio between the amplitudes of the currents applied respectively on the two loads. A way of calculating the CR is given below. Without loss of generality, all the quantities are considered normalized with respect to the average input power P_{in} of the divider, and therefore $P_{\mathrm{in}} = 1$ W. Given the value of Z_{in}, P_{in} can be expressed in terms of the complex input voltage V_{in} of the divider as follows:

$$P_{\mathrm{in}} = 0.5\left|V_{\mathrm{in}}\right|^2 \mathrm{Real}[1/Z_{\mathrm{in}}^*] \tag{7}$$

where V_{in} is the amplitude of V_{in} and $Z_{\mathrm{in}}{}^*$ is the complex conjugate value of Z_{in}. Given that $P_{\mathrm{in}} = 1$ W, the earlier equation yields:

$$V_{\mathrm{in}} = \sqrt{2/\mathrm{Real}[1/Z_{\mathrm{in}}^*]}e^{j\theta} \tag{8}$$

where θ is the phase of V_{in}. Regarding V_{in} as reference voltage, we may assume that $\theta = 0$. Thus, Eq. (8) is simplified as follows:

$$V_{\mathrm{in}} = \sqrt{2/\mathrm{Real}[1/Z_{\mathrm{in}}^*]} \tag{9}$$

V_{in} coincides with the voltages at the positions A_4 and B_4:

$$V_{\mathrm{A4}} = V_{\mathrm{B4}} = V_{\mathrm{in}} = \sqrt{2/\mathrm{Real}[1/Z_{\mathrm{in}}^*]} \tag{10}$$

Using transmission line theory [59–62], the voltages at the positions A_i ($i = 3,\ldots,0$) are calculated recursively by the following expression:

$$V_{\mathrm{Ai}} = V_{\mathrm{A}(i+1)}\left[\cos(\beta D_{\mathrm{a}(i+1)}) - j\frac{Z_{\mathrm{oa}(i+1)}}{Z_{\mathrm{A}(i+1)}}\sin(\beta D_{\mathrm{a}(i+1)})\right] \tag{11}$$

Similarly, the voltages at the positions B_i ($i = 3,\ldots,0$) are calculated recursively by the expression:

$$V_{\mathrm{Bi}} = V_{\mathrm{B}(i+1)}\left[\cos(\beta D_{\mathrm{b}(i+1)}) - j\frac{Z_{\mathrm{ob}(i+1)}}{Z_{\mathrm{B}(i+1)}}\sin(\beta D_{\mathrm{b}(i+1)})\right] \tag{12}$$

The complex currents applied respectively on the two terminal loads are calculated according to the expressions:

$$I_{\mathrm{AT}} = V_{\mathrm{A0}}/Z_{\mathrm{AT}} \tag{13}$$

$$I_{\mathrm{BT}} = V_{\mathrm{B0}}/Z_{\mathrm{BT}} \tag{14}$$

Finally, the current-split ratio is derived by:

$$\mathrm{CR} = |I_{\mathrm{AT}}|/|I_{\mathrm{BT}}| \tag{15}$$

Provided that the complex currents I_{AT} and I_{BT} have been calculated, the phase difference $\Delta\varphi$ between these currents can be derived as well.

Since the divider is optimized for multifrequency operation, the BW, CR, and $\Delta\varphi$ must be calculated for all frequencies of operation. The optimization is performed using a PSO algorithm developed by the authors. For the structure described above, the algorithm uses 16 input parameters, which are the lengths and the corresponding characteristic impedances of the eight sections that compose the divider. The objective of the algorithm is to find the values of the input parameters that maximize a suitably defined fitness function based on the requirements for the BW, CR, and $\Delta\varphi$. Thus, the fitness function is expressed by

$$F = \sum_{m=1}^{M}\left[w_m^{\mathrm{CR}}|\mathrm{CR}(f_m) - \mathrm{CR_d}(f_m)| + w_m^{\Delta\varphi}|\Delta\varphi(f_m) - \Delta\varphi_d(f_m)| + w_m^{\mathrm{RL}}\,\mathrm{RL}(f_m) + w_m^{\mathrm{BW}}\,F_m^{\mathrm{BW}}\right] \tag{16}$$

where m is the order of any resonant frequency and M is the total number of the resonant frequencies. Moreover, $\mathrm{CR}(f_m)$, $\Delta\varphi(f_m)$, and $\mathrm{RL}(f_m)$ are respectively the current-split ratio, the phase difference between the currents at the terminal points of the divider, and the return loss, all calculated at the resonant frequency f_m. $\mathrm{CR_d}(f_m)$ and $\Delta\varphi_\mathrm{d}(f_m)$ are the desired values of CR and $\Delta\varphi$ at f_m. The use of $\mathrm{RL}(f_m)$ in Eq. (16) ensures a deep resonance at f_m. The term F_m^{BW} refers to the impedance-matching BW at the resonant frequency f_m, as given below:

$$F_m^{\mathrm{BW}} = \begin{cases}\mathrm{BW}(f_m) - \mathrm{BW_d}(f_m), & \text{if } \mathrm{BW}(f_m) < \mathrm{BW_d}(f_m)\\ 0, & \text{if } \mathrm{BW}(f_m) \geq \mathrm{BW_d}(f_m)\end{cases} \tag{17}$$

where $\mathrm{BW_d}(f_m)$ is the desired value of BW at f_m. The meaning of Eq. (17) is that only values of BW less than $\mathrm{BW_d}$ have influence on the value of F_m^{BW}. Values of BW greater than or equal to $\mathrm{BW_d}$ may not affect the value of F_m^{BW}, because they satisfy the requirement for the BW. In general, F_m^{BW} has negative values and vanishes only when the desired BW is achieved. The coefficients w_m^{CR}, $w_m^{\Delta\varphi}$, w_m^{RL}, and w_m^{BW} are weight factors and they denote the importance of the corresponding terms that compose the fitness function. Provided that w_m^{CR}, $w_m^{\Delta\varphi}$, w_m^{RL} ($m = 1,\ldots,M$) have negative values and w_m^{BW} ($m = 1,\ldots,M$) have positive values, the fitness function tends to be maximized when the BW, CR, and $\Delta\varphi$ tend to reach their respective desired values.

PSO has been studied in many papers [30–39] and is briefly described in [56, 57]. According to the PSO theory, the optimization is based on the intelligence and movement of swarms. Every individual in the swarm is called "particle" and the number S of the particles is called "swarm size." A swarm size of 30 particles is used in the algorithm. The position of the ith particle ($i = 1,\ldots,S$) is represented as $\vec{x}_i = (x_{i1},\ldots,x_{iN})$, where x_{in} ($n = 1,\ldots,N$) are the position coordinates in a N-dimensional search space. Actually, these coordinates are the 16 earlier-mentioned parameters that define the geometry of the divider ($N = 16$). Each coordinate x_{in} is usually limited between a lower boundary L_n and an upper boundary U_n. The difference $R_n = U_n - L_n$ is called "dynamic range" of the nth dimension. The position of each particle is evaluated by the fitness function $F = F(\vec{x}_i)$. An increase in the fitness value means that the particle improves its position. Consequently, the best position in the search space (gbest position) $\vec{g} = (g_1,\ldots,g_N)$ is the solution to the optimization problem because it corresponds to the maximum fitness value $F_{\max} = F(\vec{g})$. After a time step, the new position of the ith particle is given by

$$\vec{x}_j(t+1) = \vec{x}_i(t) + \vec{v}_i(t+1) \tag{18}$$

$\vec{v}_i = (v_{i1},\ldots,v_{iN})$ is the velocity of the ith particle and is updated [38] by the expression

TABLE 1 Structure Characteristics of the Optimized Divider That Resonates at 900 and 1800 MHz, and Feeds Two Resistive Loads Z_{AT} = 60 Ω and Z_{BT} = 72 Ω

Example 1	Case a[a]	Case b[b]	Case c[c]
Z_{oa1}/D_{a1}	97.03 Ω/0.249 λ_0	78.89 Ω/0.227 λ_0	99.37 Ω/0.175 λ_0
Z_{oa2}/D_{a2}	102.02 Ω/0.272 λ_0	85.05 Ω/0.234 λ0	98.13 Ω/0.165 λ_0
Z_{oa3}/D_{a3}	84.186 Ω/0.155 λ_0	87.70 Ω/0.281 λ_0	147.14 Ω/0.211 λ_0
Z_{oa4}/D_{a4}	103.11 Ω/0.232 λ_0	106.61 Ω/0.129 λ_0	100.74 Ω/0.106 λ_0
Z_{ob1}/D_{b1}	119.06 Ω/0.312 λ_0	108.78 Ω/0.266 λ_0	65.23 Ω/0.255 λ_0
Z_{ob2}/D_{b2}	131.64 Ω/0.166 λ_0	98.16 Ω/0.214 λ_0	65.75 Ω/0.140 λ_0
Z_{ob3}/D_{b3}	74.52 Ω/0.204 λ_0	63.42 Ω/0.209 λ_0	61.96 Ω/0.135 λ_0
Z_{ob4}/D_{b4}	78.68 Ω/0.204 λ_0	72.86 Ω/0.180 λ_0	76.08 Ω/0.116 λ_0

[a] For case a: Frequencies: 900 and 1800 MHz; Required CR/$\Delta\phi$: 1/0° and 1/0°; Resulted CR/$\Delta\phi$: 1.000/0.0° and 1.000/0.0°, respectively.
[b] For case b: Frequencies: 900 and 1800 MHz; Required CR/$\Delta\phi$: 1/0° and 1.5/0°; Resulted CR/$\Delta\phi$: 0.999/0.0° and 1.504/0.0°, respectively.
[c] For case c: Frequencies: 900 and 1800 MHz; Required CR/$\Delta\phi$: 1.5/0° and 1/0°; Resulted CR/$\Delta\phi$: 1.500/0.0° and 1.000/0.0°, respectively.

TABLE 2 Structure Characteristics of the Optimized Divider That Resonates at 900 and 1800 MHz, and Feeds Two Complex Loads Z_{AT} = 100 + j15 Ω and Z_{BT} = 200 − j40 Ω

Example 2	Case a[a]	Case b[b]	Case c[c]
Z_{oa1}/D_{a1}	92.10 Ω/0.232 λ_0	75.56 Ω/0.220 λ_0	136.76 Ω/0.212 λ_0
Z_{oa2}/D_{a2}	114.76 Ω/0.342 λ_0	116.88 Ω/0.262 λ_0	112.46 Ω/0.152 λ_0
Z_{oa3}/D_{a3}	107.27 Ω/0.280 λ_0	153.60 Ω/0.312 λ_0	89.63 Ω/0.267 λ_0
Z_{oa4}/D_{a4}	107.17 Ω/0.225 λ_0	129.63 Ω/0.285 λ_0	143.26 Ω/0.217 λ_0
Z_{ob1}/D_{b1}	129.37 Ω/0.161 λ_0	157.52 Ω/0.161 λ_0	133.68 Ω/0.122 λ_0
Z_{ob2}/D_{b2}	101.66 Ω/0.354 λ_0	106.52 Ω/0.283 λ_0	100.27 Ω/0.290 λ_0
Z_{ob3}/D_{b3}	135.69 Ω/0.280 λ_0	107.00 Ω/0.352 λ_0	124.58 Ω/0.270 λ_0
Z_{ob4}/D_{b4}	97.24 Ω/0.295 λ_0	79.93 Ω/0.289 λ_0	101.51 Ω/0.173 λ_0

[a] For case a: Frequencies: 900 and 1800 MHz; Required CR/$\Delta\phi$: 1/0° and 1/0°; Resulted CR/$\Delta\phi$: 1.000/0.0° and 1.000/0.0°, respectively.
[b] For case b: Frequencies: 900 and 1800 MHz; Required CR/$\Delta\phi$: 1/0° and 1.5/0°; Resulted CR/$\Delta\phi$: 1.000/0.0° and 1.500/0.0°, respectively.
[c] For case c: Frequencies: 900 and 1800 MHz; Required CR/$\Delta\phi$: 1.5/0° and 1/0°; Resulted CR/$\Delta\phi$: 1.500/0.0° and 1.000/0.0°, respectively

$$\vec{v}_i(t+1) = k\{\vec{v}_i(t) + \varphi_1 \,\text{rand}(t)[\vec{p}_i(t) - \vec{x}_i(t)] + \varphi_2 \,\text{rand}(t)\,[\vec{\ell}_i(t) - \vec{x}_i(t)]\} \quad (19)$$

where $\vec{p}_i = (p_{il},\cdots,p_{iN})$ is the best previous position (pbest position) of the ith particle, $\vec{\ell}_i = (\ell_{i\ell},\cdots,\ell_{iN})$ is the best position (lbest position) found so far by the K_i neighbors of the ith particle, and rand (t) is a uniform random number generator. Three neighbors per particle ($K_i = 3$) is a good choice for many problems. In addition, the parameter k is the "constriction coefficient" and is defined by the expression

$$k = \frac{2}{|2 - \varphi - \sqrt{\varphi^2 - 4\varphi}|} \quad (20)$$

The parameter $\varphi = \varphi_1 + \varphi_2$ is called "acceleration constant" and must be greater than four. A good choice for both φ_1 and φ_2 is 2.05 [36]. Thus, $\varphi = 4.10$ and $k = 0.73$. To keep the particles in bounds, it is better to define a maximum allowed velocity $\vec{v}_{\max} = (v_{\max,1},\ldots,v_{\max,N})$. Each coordinate of this velocity is set to $v_{\max,n} = 0.10R_n$ ($n = 1,\ldots,N$). Therefore, for each ith particle and each nth dimension, if $v_{in} > v_{\max,n}$ then $v_{in} = v_{\max,n}$, and also if $v_{in} < -v_{\max,n}$ then $v_{in} = -v_{\max,n}$. However, $\vec{v}_{\max}$ and k are not able to confine the particles within the search space. To solve this problem, a boundary condition called "absorbing walls" is used in the PSO algorithm. According to this condition, if $x_{in} > U_n$ then $x_{in} = U_n$ and $v_{in} = 0$, and also if $x_{in} < L_n$ then $x_{in} = L_n$ and $v_{in} = 0$. Finally, a brief description of the structure of the PSO algorithm can be found in [56, 57].

3. RESULTS

The proposed technique was initially applied at the mobile communications frequencies of 900 and 1800 MHz, to optimize the divider for GSM/DCS operation. Two unequal resistive loads Z_{AT} = 60 Ω and Z_{BT} = 72 Ω are assumed to be connected at the terminal points of the divider. Three cases are studied in this example concerning different values of current-split ratio: (a) CR = 1 at both frequencies, (b) CR = 1 at 900 MHz and CR = 1.5 at 1800 MHz, (c) CR = 1.5 at 900 MHz and CR = 1 at 1800 MHz. In all the earlier cases, the currents at the terminal points of the divider are required to be in phase ($\Delta\varphi = 0$). The results of the three cases are summarized in Table 1, while the frequency re-

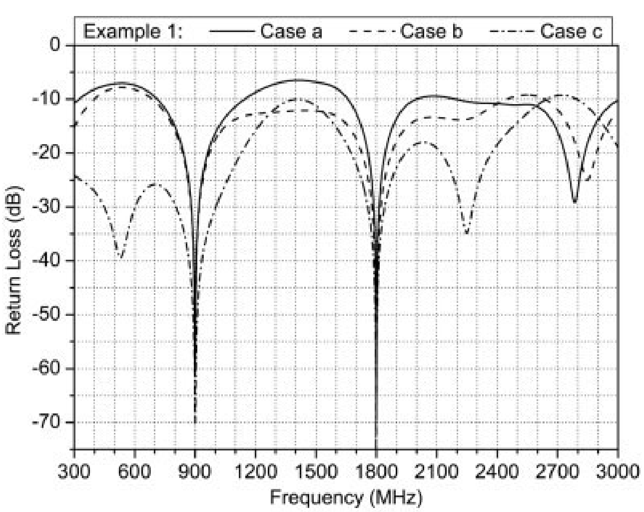

Figure 2 Frequency response of the optimized divider that resonates at 900 and 1800 MHz, and feeds two resistive loads Z_{AT} = 60 Ω and Z_{BT} = 72 Ω

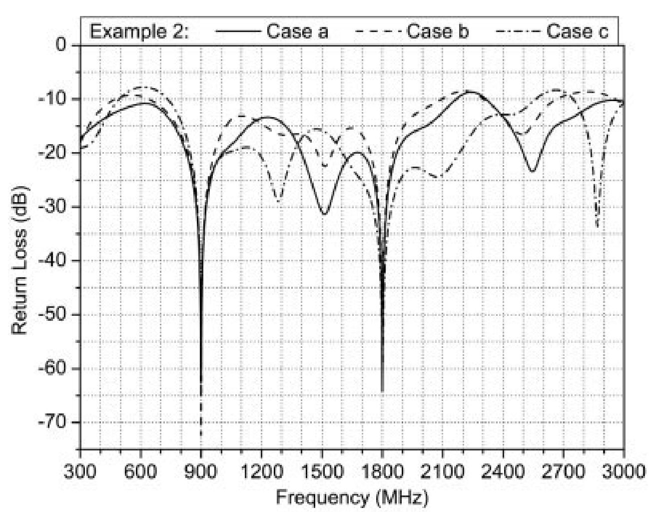

Figure 3 Frequency response of the optimized divider that resonates at 900 and 1800 MHz, and feeds two complex loads Z_{AT} = 100 + j15 Ω and Z_{BT} = 200 − j40 Ω

TABLE 3 Structure Characteristics of the Optimized Divider That Resonates at 900, 1800, 1900, and 2050 MHz, and Feeds Two Resistive Loads Z_{AT} = 60 Ω and Z_{BT} = 72 Ω

Example 3	Case a[a]	Case b[b]
Z_{oa1}/D_{a1}	79.34 Ω/0.122 λ_0	55.40 Ω/0.449 λ_0
Z_{oa2}/D_{a2}	114.36 Ω/0.186 λ_0	69.67 Ω/0.325 λ_0
Z_{oa3}/D_{a3}	125.88 Ω/0.268 λ_0	99.63 Ω/0.330 λ_0
Z_{oa4}/D_{a4}	97.42 Ω/0.241 λ_0	150.51 Ω/0.343 λ_0
Z_{ob1}/D_{b1}	80.92 Ω/0.118 λ_0	71.88 Ω/0.465 λ_0
Z_{ob2}/D_{b2}	97.78 Ω/0.195 λ_0	72.18 Ω/0.283 λ_0
Z_{ob3}/D_{b3}	98.19 Ω/0.273 λ_0	71.65 Ω/0.353 λ_0
Z_{ob4}/D_{b4}	84.55 Ω/0.231 λ_0	69.86 Ω/0.345 λ_0

[a] For case a: Frequencies: 900, 1800, 1900, and 2050 MHz; Required CR/Δϕ: 1/0°, 1/0°, 1/0°, and 1/0°; Resulted CR/Δϕ: 1.000/−0.5°, 0.995/0.0°, 1.006/0.0°, and 1.000/0.0°, respectively.

[b] For case b: Frequencies: 900, 1800, 1900, and 2050 MHz; Required CR/Δϕ: 1.5/0°, 1.5/0°, 1.5/0°, and 1.5/0°; Resulted CR/Δϕ: 1.500/0.4°, 1.500/0.0°, 1.500/0.0°, and 1.500/0.0°, respectively.

TABLE 4 Structure Characteristics of the Optimized Divider that Resonates at 900, 1800, 1900, and 2050 MHz, and Feeds Two Complex Loads Z_{AT} = 100 + j15 Ω and Z_{BT} = 200 − j40 Ω

Example 4	Case a[a]	Case b[b]
Z_{oa1}/D_{a1}	106.68 Ω/0.207 λ_0	123.03 Ω/0.222 λ_0
Z_{oa2}/D_{a2}	80.38 Ω/0.285 λ_0	78.72 Ω/0.289 λ_0
Z_{oa3}/D_{a3}	90.64 Ω/0.187 λ_0	93.50 Ω/0.174 λ_0
Z_{oa4}/D_{a4}	123.69 Ω/0.110 λ_0	181.24 Ω/0.145 λ_0
Z_{ob1}/D_{b1}	135.52 Ω/0.111 λ_0	155.44 Ω/0.093 λ_0
Z_{ob2}/D_{b2}	77.24 Ω/0.184 λ_0	112.08 Ω/0.252 λ_0
Z_{ob3}/D_{b3}	61.90 Ω/0.275 λ_0	100.82 Ω/0.361 λ_0
Z_{ob4}/D_{b4}	84.02 Ω/0.239 λ_0	74.97 Ω/0.134 λ_0

[a] For case a: Frequencies: 900, 1800, 1900, and 2050 MHz; Required CR/Δϕ: 1/0°, 1/0°, 1/0°, and 1/0°; Resulted CR/Δϕ: 1.000/0.0°, 1.000/0.0°, 1.002/−2.1°, and 1.000/0.0°, respectively.

[b] For case b: Frequencies: 900, 1800, 1900, and 2050 MHz; Required CR/Δϕ: 1.5/0°, 1.5/0°, 1.5/0°, and 1.5/0°; Resulted CR/Δϕ: 1.500/0.4°, 1.500/0.0°, 1.498/−2.1°, and 1.500/0.0°, respectively.

sponse of the divider is presented in Figure 2. Specifically, the tables of all the examples show the required and the resulted values of CR and Δφ, as well as the characteristic impedances and the lengths of the sections derived from the optimization procedure. All the lengths are measured in terms of a reference wavelength λ_0, which is the wavelength inside the structure of the divider at 900 MHz. It is obvious that the frequency response of the resulting divider satisfies the requirements for GSM/DCS operation.

The technique was also applied at 900 and 1800 MHz considering two unequal complex terminal loads $Z_{AT} = 100 + j15$ Ω and $Z_{BT} = 200 - j40$ Ω. The same three cases are also studied in this example and Δφ is required to be equal to zero in all these cases. The results are given in Table 2, while Figure 3 exhibits an excellent frequency response. It is well known that the complex loads are more destructive to the matching condition than the resistive loads. However, the particle swarm optimizer is capable of finding a very broadband structure, which is suitable for GSM/DCS operation.

The next example is an effort to optimize the divider for GSM/DCS/PCS/UMTS operation. Therefore, the divider must resonate at 900, 1800, 1900, and 2050 MHz. The same unequal resistive loads $Z_{AT} = 60$ Ω and $Z_{BT} = 72$ Ω are assumed to be the terminal loads of the divider. Two cases are studied in this example: (a) CR = 1 and Δφ = 0 at all the above four frequencies, and (b) CR = 1.5 and Δφ = 0 at all the above four frequencies. The results are summarized in Table 3, while the frequency response of the divider is presented in Figure 4. Despite the fact that the terminal loads are not matched to the main feeding line, the optimization procedure is capable of finding a broadband structure, which is suitable for GSM/DCS/PCS/UMTS operation.

The last example is another effort to optimize the divider for GSM/DCS/PCS/UMTS operation, considering two unequal complex loads $Z_{AT} = 100 + j15$ Ω and $Z_{BT} = 200 - j40$ Ω connected at the terminal points of the divider. The two cases studied in the previous example are also studied here. The results are given in Table 4, while Figure 5 exhibits a very broadband structure that satisfies the requirements for GSM/DCS/PCS/UMTS operation.

4. CONCLUSIONS

Despite the initial requirements for GSM/DCS or GSM/DCS/PCS/UMTS operation, our technique results in very broadband struc-

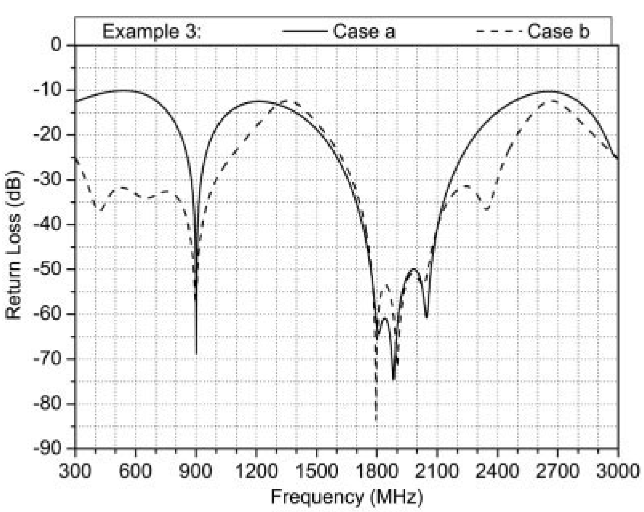

Figure 4 Frequency response of the optimized divider that resonates at 900, 1800, 1900, and 2050 MHz, and feeds two resistive loads Z_{AT} = 60 Ω and Z_{BT} = 72 Ω

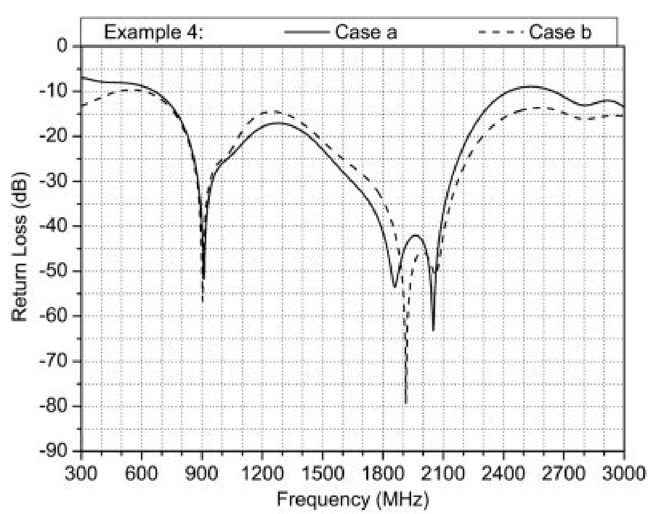

Figure 5 Frequency response of the optimized divider that resonates at 900, 1800, 1900, and 2050 MHz, and feeds two complex loads Z_{AT} = 100 + j15 Ω and Z_{BT} = 200 − j40 Ω

tures. Moreover, the technique has the ability to satisfy simultaneously many requirements at many frequencies, considering that the terminal loads are not matched to the main transmission line that feeds the divider. Therefore, the efficiency of the proposed technique exceeds our expectations. In addition, the proposed structure of the divider is compact and simple. The optimized structures can be fabricated by using microstrip technology, and thus they can be effectively used in many practical applications.

REFERENCES

1. K. Chang, RF and microwave wireless systems, Wiley, New York, 2000.
2. K. Fujimoto and J.R. James, Mobile antenna systems handbook, 2nd ed., Artech House, Norwood, MA, 2001.
3. W.C.Y. Lee, Wireless and cellular communications, 3rd ed., McGraw-Hill, New York, 2006.
4. L.G. Maloratsky, Passive RF and microwave integrated circuits, Elsevier, Burlington, MA, 2004.
5. K. Chang, M. Li, K. A. Hummer, and R.A. Speciale, High power four-way power divider/combiner, IEEE MTT-S Int Microwave Symp Dig 3 (1990), 1329-1332.
6. L. Fan and K. Chang, Uniplanar MIC power dividers using coupled CPW and asymmetrical CPS, IEEE MTT-S Int Microwave Symp Dig 2 (1996), 781-784.
7. L. Fan and K. Chang, Uniplanar power dividers using coupled CPW and asymmetrical CPS for MIC's and MMIC's, IEEE Trans Microwave Theory Tech 44 (1996), 2411-2420.
8. L. Fan and K. Chang, A 180° out-of-phase power divider using asymmetrical coplanar stripline, IEEE Microwave Guided Wave Lett 6 (1996), 404-406.
9. P. Rigoland, M. Drissi, C. Terret, and P. Gadenne, Power divider topologies applied to antenna synthesis, Microwave Opt Technol Lett 12 (1996), 167-171.
10. N.C. Karmakar and M.E. Bialkowski, Design of multistage multiway microstrip fork power dividers, Microwave Opt Technol Lett 23 (1999), 141-147.
11. S. Ray and G. Kumar, Three-port rectangular microstrip unequal power divider and coupler, Microwave Opt Technol Lett 29 (2001), 219-223.
12. Kam Mam Shum, Quan Xue, Wing Nam Chau, and Chi Hou Chan, A compact Wilkinson power divider with curved PBG cells, Microwave Opt Technol Lett 31 (2001), 81-83.
13. I. Gómez, L. De Haro, B. Galocha, and J.L. Besada, Optimized power dividers based on E-plane T-junctions, Microwave Opt Technol Lett 31 (2001), 118-123.
14. T.-Y. Yun, C. Wang, P. Zepeda, C. T. Rodenbeck, M. R. Coutant, M.-Y. Li, and K. Chang, A 10- to 21-GHz, low-cost, multifrequency, and full-duplex phased-array antenna system, IEEE Trans Antennas Propag 50 (2002), 641-650.
15. L. Álvarez, J. Portilla, M.L. De la Fuente, and E. Artal, MMIC medium-power amplifier in K band with matching and power-divider/combiner networks implemented with the use of lumped elements, Microwave Opt Technol Lett 33 (2002), 397-400.
16. J.-H. Bang, S.-M. Hwang, S.-G. Lee, B.-C. Ahn, Design formulas for the H-plane septum power divider in a rectangular waveguide, Microwave Opt Technol Lett 37 (2003), 390-393.
17. Y. Yuan, C.H. Chan, and K.F. Man, Design of unequal microstrip power divider using hierarchal genetic algorithm, Microwave Opt Technol Lett 37 (2003), 421-423.
18. C.-C. Huang, C.-Y. Chang, and W.-S. Wang, Single-mode four-branch power divider with coupled wide-angle waveguides, Microwave Opt Technol Lett 38 (2003), 337-341.
19. C. Lim, R.K. Settaluri, V.K. Tripathi, and A. Weisshaar, Compact single-level and multilevel folded-line RF power dividers, Microwave Opt Technol Lett 39 (2003), 187-189.
20. S.C. Hui, B.L. Ooi, H.Y. Fong, and B. Wu, Broadband multilayer active-slot power divider, Microwave Opt Technol Lett 41 (2004), 10-12.
21. T. Kangasvieri, I. Hautajärvi, H. Jantunen, and J. Vähäkangas, Miniaturized low-loss Wilkinson power divider for RF front-end module applications, Microwave Opt Technol Lett 48 (2006), 660-663.
22. J. Li, Y. Zou, and S. He, A novel power divider utilizing composite right/left-handed transmission line, Microwave Opt Technol Lett 48 (2006), 1776-1779.
23. J.-Z. Gu, X.-J. Yu, and X.-W. Sun, A compact harmonic-suppressed Wilkinson power divider using C-SCMRC resonators, Microwave Opt Technol Lett 48 (2006), 2382-2384.
24. A.M. Elboshy, E.K. El-Kinawy, E.A.F. Abdallah, and H. El-Hinawy, Novel formula for designing microstrip circular sector power divider and its application in antenna arrays, WSEAS Trans Commun 5 (2006), 1869-1876.
25. A.-L. Perrier, J.-M. Duchamp, and P. Ferrari, A small-size semilumped three-port tunable power divider, Microwave Opt Technol Lett 49 (2007), 90-94.
26. K. Song, Y. Fan, and Y. Zhang, Broad-band power divider based on radial waveguide, Microwave Opt Technol Lett 49 (2007), 595-597.
27. J. Li and Y. Zou, Novel Wilkinson power divider based on left-handed transmission lines, Microwave Opt Technol Lett 49 (2007), 712-715.
28. D.G. Kampitaki, A.T. Hatzigaidas, A.I. Papastergiou, and Z.D. Zaharis, On the design of a dual-band unequal power divider useful for mobile communications, Elect Eng (2006), DOI 10.1007/s00202-006-0024-4.
29. D. Kampitaki, A. Hatzigaidas, A. Papastergiou, P. Lazaridis, and Z. Zaharis, Dual-frequency splitter synthesis suitable for practical RF applications, WSEAS Trans Commun 5 (2006), 1885-1891.
30. J. Kennedy, and R.C. Eberhart, Particle swarm optimization, IEEE Conf Neural Networks 4 (1995), 1942-1948.
31. Y. Shi, and R.C. Eberhart, A modified particle swarm optimizer, IEEE Congr Evolut Comput (1998), 69-73.
32. Y. Shi, and R.C. Eberhart, Parameter selection in particle swarm optimization, in 7th Annual Conf Evolut Program (1998), 591-600.
33. J. Kennedy, Small worlds and mega-minds—Effects of neighborhood topology on particle swarm performance, IEEE Congr Evolut Comput 3 (1999), 1931-1938.
34. Y. Shi and R.C. Eberhart, Empirical study of particle swarm optimization, IEEE Congress Evolut Computation 3 (1999), 1945-1950.
35. J. Kennedy, Stereotyping: Improving particle swarm performance with cluster analysis, IEEE Congr Evolut Comput 2 (2000), 1507-1512.
36. R.C. Eberhart and Y. Shi, Particle swarm optimization—developments, applications and resources, IEEE Congr Evolut Comput 1 (2001), 81-86.
37. J. Kennedy, R.C. Eberhart, and Y. Shi, Swarm intelligence, Morgan Kaufmann, 2001.
38. M. Clerc and J. Kennedy, The particle swarm—explosion, stability, and convergence in a multidimensional complex space, IEEE Trans Evolut Comput 6 (2002), 58-73.
39. R.C. Eberhart and Y. Shi, Comparing inertia weights and constriction factors in particle swarm optimization, IEEE Congr Evolut Comput 1 (2002), 84-88.
40. J.R. Pérez and J. Basterrechea, Particle-swarm optimization and its application to antenna far-field-pattern prediction from planar scanning, Microwave Opt Technol Lett 44 (2005), 398-403.
41. S. Mikki and A. Kishk, Improved particle swarm optimization technique using hard boundary conditions, Microwave Opt Technol Lett 46 (2005), 422-426.
42. A.I.F. Vaz, A.I.P.N. Pereira, and E.M.G.P. Fernandes, Particle swarm and simulated annealing for multi-global optimization, WSEAS Trans Inform Sci Appl 2 (2005), 534-539.
43. F. Azevedo and Z.A. Vale, Optimal short-term contract allocation using particle swarm optimization, WSEAS Trans Inform Sci Appl 2 (2005), 552-558.
44. C. Jiang, Y. Ma, Y. Song, Y. Liu, J. Lu, and L. Wang, Short-Term power load forecasting using combination model with improved particle swarm optimization, WSEAS Trans Inform Sci Appl 2 (2005), 853-858.
45. A. Kalos, Discrete particle swarm optimization for automating the design of multivariate autoregressive neural networks, WSEAS Trans Inform Sci Appl 2 (2005), 1807-1815.
46. Y. Yang, R.S. Chen, and Z.B. Ye, Combination of particle-swarm optimization with least-squares support vector machine for FDTD time series forecasting, Microwave Opt Technol Lett 48 (2006), 141-144.

47. A. Akdagli, and K. Guney, New wide-aperture-dimension formula obtained by using a particle swarm optimization for optimum gain pyramidal horns, Microwave Opt Technol Lett 48 (2006), 1201-1205.
48. S. Xu, Y. Rahmat-Samii, and D. Gies, Shaped-reflector antenna designs using particle swarm optimization: An example of a direct-broadcast satellite antenna, Microwave Opt Technol Lett 48 (2006), 1341-1347.
49. R. Azaro, F. De Natale, M. Donelli, and A. Massa, Particle-swarm-optimizer-based optimization of matching loads for lossy transmission lines, Microwave Opt Technol Lett 48 (2006), 1485-1487.
50. S.K. Goudos and J.N. Sahalos, Microwave absorber optimal design using multi-objective particle swarm optimization, Microwave Opt Technol Lett 48 (2006), 1553-1558.
51. R. Azaro, M. Donelli, D. Franceschini, E. Zeni, and A. Massa, Optimized synthesis of a miniaturized SARSAT band pre-fractal antenna, Microwave Opt Technol Lett 48 (2006), 2205-2207.
52. J. Horák, P. Chmela, L. Oliva, and Z. Raida, Multiband planar antennas on electromagnetic bandgap substrates: Complex global optimization of the structure, Microwave Opt Technol Lett 48 (2006), 2532-2534.
53. H. Yan and R. Ma, A multiobjective particle swarm optimization approach and application in multiobjective electricity power dispatch, WSEAS Trans Inform Sci Appl 3 (2006), 1288-1293.
54. B.S. Al-Kazemi, Velocity analysis for particle swarm optmization, WSEAS Trans Inform Sci Appl 3 (2006), 1807-1815.
55. S.K. Goudos, A versatile software tool for microwave planar radar absorbing materials design using global optimization algorithms, Mater Des (2006), DOI 10.1016/j.matdes. 2006.10.016.
56. Z. Zaharis, D. Kampitaki, A. Papastergiou, A. Hatzigaidas, P. Lazaridis, and M. Spasos, Optimal design of a linear antenna array under the restriction of uniform excitation distribution using a particle swarm optimization based method, WSEAS Trans Commun 6 (2007), 52-59.
57. Z.D. Zaharis, D.G. Kampitaki, P.I. Lazaridis, A.I. Papastergiou, A.T. Hatzigaidas, and P.B. Gallion, Improving the radiation characteristics of a base station antenna array using a particle swarm optimizer, Microwave Opt Technol Lett ,in press.
58. S.K. Goudos, Application of a particle swarm optimizer to the design of microwave broadband absorbers, WSEAS Trans Commun 6 (2007), 312-317.
59. R.E. Collin, Foundations for microwave engineering, 2nd ed., Wiley-IEEE Press, New York, 2000.
60. K. Chang, I. Bahl, and V. Nair, RF and microwave circuit and component design for wireless systems, Wiley, New York, 2002.
61. K. Chang, Handbook of RF/microwave components and engineering, Wiley, Hoboken, NJ, 2003.
62. D.M. Pozar, Microwave engineering, 3rd ed., Wiley, New York, 2004.

TUNABLE (BA, SR)TIO$_3$ INTERDIGITAL CAPACITOR ONTO SI WAFER FOR RECONFIGURABLE RADIO

Ki-Byoung Kim,[1,2,3] Tae-Soon Yun,[2] Jong-Chul Lee,[2] Mohamed Chaker,[4] and Ke Wu[3]
[1] Intelligent Radio Engineering Center, Information and Communication University, 103-6 Munji-dong, Yuseong-Gu, Daejeon 305-732, Korea
[2] RFIC Research and Education Center, Kwangwoon University, 447-1 Wolgye-dong, Nowon-Gu, Seoul 139-701, Korea
[3] Poly-Grames Research Center, Ecole Polytechnique, Montreal, QC, H3V 1A2, Canada
[4] INRS-Energie, Mareriaux et Telecommunication, Varennes, QC, J3X 1S2, Canada

Received 19 February 2007

ABSTRACT: *In this article, the potential feasibility of integrating BST films into Si wafer by adopting tunable interdigital capacitor (IDC) with TiO_2 thin film buffer layer is suggested. TiO_2 as buffer layer is grown onto Si substrate by atomic layer deposition and the coplanar IDC on $Ba_xSr_{1-x}TiO_3$(500 nm)/TiO_2(50 nm)/high resistivity Si (HR-Si) is fabricated. BST interdigital tunable capacitors integrated on HR-Si substrate with high tunability and low loss tangent are characterized for their microwave performances. BST/HR-Si and BST/TiO_2/HR-Si IDCs show much enhanced tunability values of 31% and 40%, respectively as compared to the value of 21% obtained with BST film on MgO single crystal substrate at the bias of 5 kV/cm. BST/TiO_2/HR-Si structure shows much improved figure of merit of 504.4 as compared to 418.53 and 101.68 of BST/MgO and BST/HR-Si structure, respectively.* © 2007 Wiley Periodicals, Inc. Microwave Opt Technol Lett 49: 2144–2148, 2007; Published online in Wiley InterScience (www.interscience.wiley.com). DOI 10.1002/mop.22657

Key words: *tunable capacitor; $Ba_xSr_{1-x}TiO_3$; ferroelectric; interdigital capacitor*

1. INTRODUCTION

In the recent wireless communication system field, a great diversity of networks such as cellular network, personal area network, wireless local area network, satellite, ultra-wide band, ubiquitous, and optical network coexist. To realize global roaming, both for voice and data application, all of these standards need to be included in a various service radio terminal. Therefore, a compact and low cost tunable device is indispensable for intelligent RF applications satisfying multi-band or multi-mode standard. Tunable dielectric-based RF device technology is one of the suitable solutions for intelligent RF applications. Specially, barium strontium titanate, $Ba_{1-x}Sr_xTiO_3$ (BST), is being investigated with considerable interest as a dielectric material for tunable microwave device applications because of its large field dependent permittivity, high dielectric constant, and relatively low loss tangent. By using these advantageous properties of BST, a number of advanced high frequency tunable capacitors have been successfully demonstrated and integrated into RF components, such as phase shifters, RF filters, and oscillators, because of its large field dependent permittivity, high dielectric constant, and relatively low loss tangent [1, 2]. Today, the fabrication of BST-based tunable devices have been done with only available in a small size geometry and single crystal substrates such as MgO and $LaAlO_3$, which can provide low insertion loss, good lattice match, and good mechanical support. As microwave integrated circuits largely rely on Si technology with its low cost, large area, and high volume production, there are of significant interests for BST based high frequency devices onto Si substrate [3]. However, practical applications of BST tunable devices on Si substrates are suppressed owing to the high microwave losses related to the low resistivity of Si and formation of low-K SiO_2 by the reaction between the top BST and Si substrate. In addition, high microwave insertion losses related to low resistivity Si have served as a barrier against the realization of BST and related device integration with Si microelectronics. To solve these problems, first, high resistivity Si (HR-Si) is required as the substrate for the minimization of microwave insertion losses. Second, suitable oxide buffer layers are required between the top BST layers and Si substrates to control the orientation and quality of the BST films. Our previous work, which was focused on the low-frequency dielectric properties of BST film grown on a Si substrate with a TiO_2 buffer layer grown by atomic layer deposition (ALD) at a low temperature of 220°C, demonstrated that the TiO_2 buffer layer significantly increased the tunablity of the BST film and minimized power loss via the Si substrates [1, 2].

In this article, we report on high tunability and improved microwave loss properties of BST films on HR-Si by the insertion of ALD-grown TiO_2 buffer layer. The nonlinear dielectric prop-